Eur. J. Mineral.
2005, **17**, 399-409

Investigation of loaded halite-SiO_2 interfaces undergoing dissolution-precipitation processes

GUNTRAM JORDAN[1,*], THOMAS LOHKÄMPER[1], MARTIN SCHELLEWALD[2] and WOLFGANG W. SCHMAHL[1]

[1]Institut für Geologie, Mineralogie und Geophysik, Ruhr-Universität Bochum, D-44780 Bochum, Germany
[2]Institut für Werkstoffe, Ruhr-Universität Bochum, D-44780 Bochum, Germany

Abstract: Deformation assisted by transport in aqueous solutions is important for the rheology of earth materials, and models commonly used to describe deformation by dissolution-precipitation creep assume a steady state process in a closed system which is driven by the potential energy of the system. Here, we studied the effect of uni-axial stress on the convergence of halite crystals in contact to SiO_2 at dry conditions and in presence of saturated solution by optical interferometry. Adding saturated solution caused the convergence to increase strongly. Simultaneously, Linnik-based phase shift interference microscopy was used to in situ monitor the nano-scale morphology of the loaded surface of the crystal. These investigations revealed that the measured crystal convergence is not dominated by dissolution within the loaded halite-SiO_2 interface but rather by an increased plasticity of the halite crystal due to the addition of saturated solution.

Temporarily reducing the stress reduces the elastic strain energy of the crystal and potential energy of the system as driving force for dissolution, but increases the potentiality for material transport from the interface into the bulk fluid. Thus, mechanisms which cause a remanent excess energy contribute to increased solubility and material flux during periods of reduced stress. Local plastic deformation satisfies this condition. We expect from our results that episodic cycling of tectonic stress, pore pressure, or solute activity significantly enhances deformation rates in rocks.

Key-words: dissolution-precipitation, interface, interferometer, deformation, halite.

Introduction

Common patterns such as pitted pebbles, stylolites, truncated fossils, elongated quartz grains, crenulation cleavage, and crystallization in pressure shadows are assumed to be caused by dissolution-precipitation creep DPC (Sorby, 1863; Giles, 1932; Heald, 1956; Trurnit, 1968; Durney, 1972; Gratier *et al*., 1999; Stöckhert *et al*., 1999; Sinha-Roy, 2002). In all these cases, uni-axial stress is considered to cause local variations of the chemical potential of the components of the solid in the solution (*e.g*., Paterson, 1973; McClay, 1977; Shimizu, 1995). Assuming local equilibrium the proposed mechanism of DPC comprises of i) dissolution at sites with high chemical potential (*e.g.*, the loaded grain-to-grain contacts), ii) transport of dissolved material, and iii) precipitation at sites with low chemical potential (*e.g.*, the grain-to-pore contacts or hydrostatically stressed solids within the systems).

Gibbs (1906) considered the thermodynamics of non-hydrostatically stressed solids in solutions. For a uni-axially stressed solid cube with the principal stress axis $i = x, y, z$ perpendicular to the surfaces of the solid, the molar chemical potential for the solvate forming the solid in equilibrium with face i is $\mu_i = u_i - Ts_i + p_i v_i$, where the molar quantities volume, internal energy and entropy refer to the state of the non-hydrostatically stressed solid. This uni-axial stressed state can then be compared with the hydrostatically stressed state (denoted by subscript p) by

$$\mu_i - \mu_p = u_i - u_p - Ts_i + Ts_p + p_i v_i - p v_p \quad (1).$$

This equation gives the total work for transferring the solid from the hydrostatic stress state p to the non-hydrostatic stress state. From this equation it can be inferred (Gibbs, 1906) that solutions in contact with crystalline solids subjected to distorting stresses are supersaturated with respect to the same solid under hydrostatic pressure.

Paterson (1973) rewrote Gibb's (1906) equations by stating for the chemical potential of hydrostatically stressed solids $\mu_p = u_p - Ts_p + p v_p$ and for non-hydrostatically stressed solids $\mu_s = u_s - Ts_s + \sigma_n v_s$ (σ_n = stress component normal to the surface). The difference yields:

$$\mu_s - \mu_p = (u_s - Ts_s) - (u_p - Ts_p) + \sigma_n(v_s - v_p) + (\sigma_n - p)v_p \quad (2).$$

Paterson pointed out that the influences of all parameters are small in comparison to the last term (unless $\sigma_n \approx p$). Thus, Paterson assumed that the thermodynamic driving force of DPC is dominated by this work term which basi-

*E-mail: guntram.jordan@rub.de

0935-1221/05/0017-0399 $ 4.95
DOI: 10.1127/0935-1221/2005/0017-0399

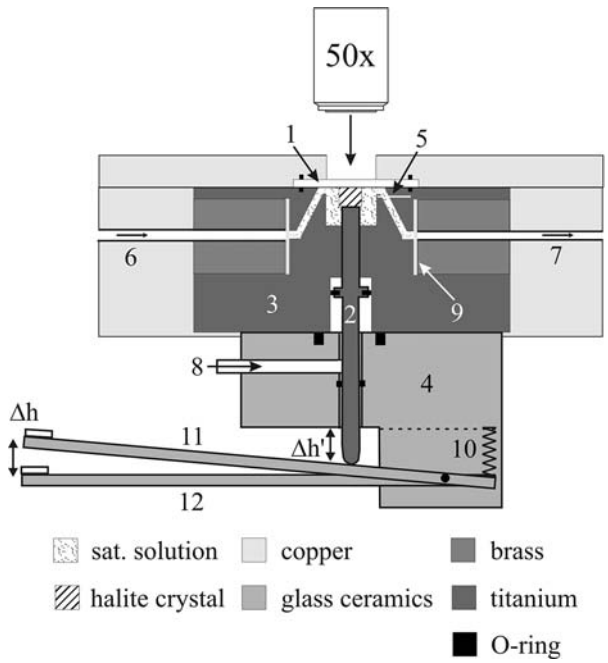

Fig. 1. Scheme of the cell. The crystal is pressed against a SiO_2-coated sapphire window (1) by a piston (2) which is loaded with compressed nitrogen. The outer diameter of the titanium cell (3) is 30 mm, the diameter of the piston is 2 mm. At the cell bottom the device for measuring the vertical position of piston can be seen (4). Further parts: temperature sensor (5), inlet (6), outlet (7), nitrogen supply (8), diaphragm (9), spring (10), sample lever (11), reference lever (12).

cally represents the reduction in potential energy of the system.

While Paterson compares the loaded and the free surfaces of one and the same crystal, Gibbs compares a non-hydrostatically and a hydrostatically stressed solid. However, both approaches come to a comparable result. The non-hydrostatically stressed crystal is in equilibrium with a more concentrated solution than a crystal stressed hydrostatically at the same pressure of the liquid. For the non-hydrostatically stressed crystal, different surfaces may differ in their chemical potential.

Since transport is part of the process, kinetic factors (detachment rates, fluxes, and growth rates) are likely to influence DPC significantly. The presence of fluid within the interfaces is a prerequisite and transport constraints e.g. within loaded interfaces may reduce the material flux considerably. However, the interface morphology as well as the fluid distribution within the interface are still unclear and, therefore, kinetic constraints remain a matter of debate (Weyl, 1959; Rutter, 1976; Raj & Chyung, 1981; Hickman & Evans, 1991, 1995; Schwarz & Stöckhert, 1996; den Brok, 1998; Schutjens & Spiers, 1999; Dysthe *et al*., 2002).

Besides influencing transport, the morphology of the interface also significantly influences the energy gradients occurring in stressed crystals. Loaded point contacts in the interface cause an inhomogeneous distribution of stress resulting in inhomogeneous elastic energy or even local zones of plastic deformation. Moreover, even extended and perfectly flat interfaces give rise to inhomogeneous elastic energy distribution within stressed solids if differences of elastic constants across interfaces and friction are present. Several different models for the morphology of the interface exist. Three should be mentioned briefly.

i) In the fluid-film model, a continuous fluid film is supposed to extend over the entire contact (Weyl, 1959; Rutter, 1976; Hickman & Evans, 1991). Gradients in chemical potential due to inhomogeneous distributions of stress are assumed to be the driving force for diffusional mass transport within the film (Weyl 1959; Sheldon *et al*., 2003).

ii) The island-channel model (Raj & Chyung, 1981; Raj, 1982; Urai *et al*., 1986; Spiers *et al*., 1990; Spiers & Schutjens, 1990; Lehner, 1995) postulates a rough interface morphology composed of islands and channels. The islands sustain the contact between the adjacent mineral grains. In the fluid filled channels dissolved material can be transported out of the contact zone.

iii) In the microgranulation model (Ostapenko, 1968), the intergrain boundaries of stressed minerals are assumed to be subject to local plastic deformation and fracture causing an interface zone which is crushed into random micro-blocks with increased density of structural defects. The excess of free energy of these zones causes dissolution, while the porosity enables transport of the dissolved material.

Most experiments on DPC were compaction or deformation experiments on granular aggregates (*e.g*., Cox & Paterson, 1991; den Brok *et al.*, 1999; Bos *et al.*, 2000; de Meer *et al.*, 2000). These kinds of experiments can provide a compaction or deformation rate, but hardly give insights into the interface morphology under stress. In addition, some single crystal experiments were performed to measure the rate of DPC and to investigate the grain-to-grain or grain-to-pore interface (Hickman & Evans, 1991; Schutjens & Spiers, 1999; Martin *et al*., 1999; den Brok & Morel, 2001; Dysthe *et al*., 2002; Lohkämper *et al*., 2003). However, light microscopy used in many studies barely enables to quantitatively measure the morphology of the interface.

Here, we investigated the evolution of the morphology of halite-SiO_2 interfaces under constant load, after unloading, and during stress cycling. For these investigations we used a recently developed in-situ phase shift interference microscope which allows the direct observation of the loaded interface with an axial resolution in the nanometer range (Lohkämper *et al.*, 2003). Data on the morphological evolution of the interface along with data on the axial convergence of the crystal allow to address the mechanism and kinetics of dissolution precipitation creep and allow to assess the efficiency of different thermodynamic driving forces in fluid assisted deformation.

Experimental

The halite-SiO_2 interface has been investigated by a Linnik type phase shift interference microscope (PSIM).

This apparatus enables to analyze the microtopography of crystal surfaces quantitatively both in air and in liquids and it provides a quantitative access to the nanotopography of solid-(liquid-)solid interfaces. The PSIM is described in detail by Lohkämper *et al.* (2003). The experiments were performed in a cell as shown in Fig. 1. The direction of stress is parallel to the optical axis. Cell and piston are made of passivated titanium. The cell cover is an SiO_2-coated, 0.5 mm thick sapphire window (MaTeck, Germany; coating: amorphous SiO_2, Ernst Befort Wetzlar, Germany, $R_a \leq 1$ nm with R_a = the average distance of the data points from the mean plane). The whole cell is embedded in a copper block with a central bore for the observation of the loaded crystal surface. The copper block is thermostated by Peltier elements, which are controlled via two Pt-100 thermosensors, one mounted near a Peltier element, the other 200 µm apart from the sample within the cell wall. In all experiments, the temperature was either 30 ± 0.05°C or room temperature. Fluid was fed by syringes pierced through diaphragms. An additional seal of the diaphragms by silicone provides a sufficiently closed system. For the preparation of saturated NaCl-solution reagent-grade NaCl (Baker, Netherlands) and deionized water (resistivity 18 MΩ cm) were used. The solution was added after the crystals had been brought into contact with the SiO_2-coated sapphire window. Finally, uni-axial stress was applied to the crystal by the piston (Fig. 1) using compressed nitrogen. The advancing piston causes a slight increase of hydrostatic pressure in the cell. However, due to the low elastic modulus of the diaphragms the increase in pressure can be regarded as insignificant.

The change in axial length of the crystal was measured by the change in height difference Δh between two sapphire crystals which were mounted on a reference and a sample glass-ceramics lever as shown in Fig. 1. The measurement was done by white light interference microscopy (*e.g.*, Sandoz, 1996). Δh is approximately proportional to the movement of the piston $\Delta h'$ and, therefore, to the change of axial length of the crystal. Deviations of proportionality depend on the angle between the two levers and were sufficiently small in our experiments. Temperature fluctuations did not affect the measurements, because identical sapphire crystals and levers were used. Moreover, the difference in thermal expansion between the titanium piston and the mounting made of glass ceramics is smaller than 10 nm/K.

The sapphire window coated with amorphous SiO_2 is chemically inert in saturated NaCl-solutions and can bear the applied stress without plastic deformation. The coating is anti-reflective if its thickness d is chosen as $d = \lambda / 4n_f$, where λ is the wave length of the light used (555 ± 25 nm) and n_f is the refractive index of the coating (Fig. 2). The reflectivity R of the sapphire window is reduced by the SiO_2 thin-film from about 8 % (in air) to 1.2 %. Moreover, the combination sapphire/SiO_2/NaCl-solution approximately satisfies the condition $n_f = \sqrt{n_s \cdot n_g}$, with n_s and n_g as the refractive indices of the adjacent phase and the cover, respectively. This condition causes equal amplitudes of reflected light at each interface. Therefore, the intensity of the light reflected at the sapphire-SiO_2 interface is largely reduced and only a slight modulation in the amplitude of the light reflected at the halite-SiO_2 interface follows.

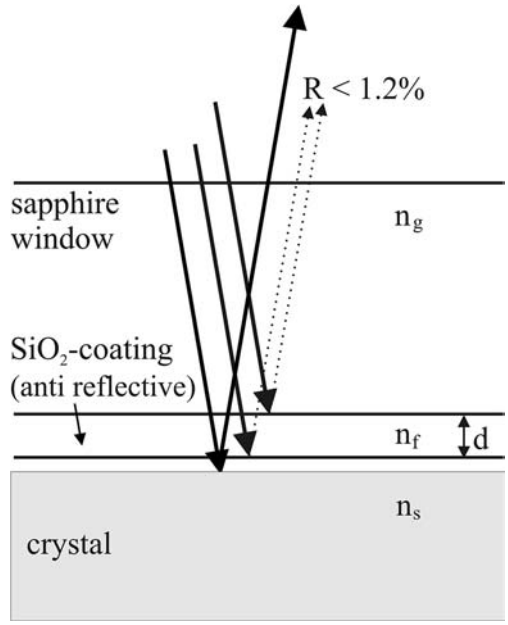

Fig. 2. An anti-reflective coating is necessary for the *in-situ* observation of the loaded interface. The optimum thickness d of the coating is a function of the wave length and the refractive indices of the window n_g, coating n_f, and sample n_s (R = reflectivity).

Synthetic halite crystals (Korth Kristalle, Germany, Young's modulus = 39.98 GPa) were used. The halite crystals (max. size 2.4 × 3.1 × 1.6 mm³) were cleaved with a scalpel parallel to all sides of {100} exposing fresh surfaces at the entire crystal immediately before mounting them into the cell. The cleavage morphology typically consisted of large cleavage steps (up to 150 nm in height), asperities, and smooth areas ($R_a \approx 10$ nm) with a size of a few thousands µm². For some experiments, Vickers indenters were applied to the (100) halite surface with loads of 0.05 N and 0.2 N for ten seconds resulting in indents with depths of *ca*. 2.8 µm and 6.3 µm, respectively. Two types of orientations were used: the square edges of the pyramid base oriented parallel <100> and <110>.

Results

Morphology of the halite-SiO_2 interface

Figure 3 shows the halite-SiO_2 interface dry and in saturated NaCl-solution. In both cases, the halite-SiO_2 interface consists of two different regions, a contact area and a non-contact area. The boundary between these two regions is marked by the first dark interference fringe, where the distance between the SiO_2 surface and the halite surface corresponds to λ/4 (≈ 138 nm). The contact area and the non-contact area together represent the total interface area. With respect to the total interface area of about 0.2 mm² in Fig. 3, the nominal uni-axial stress on the dry and the wet

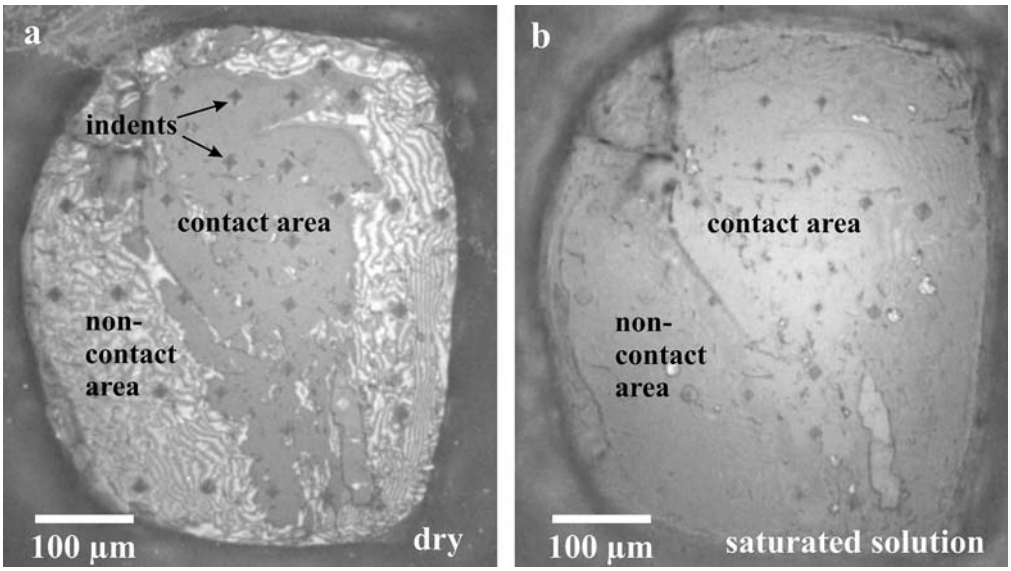

Fig. 3. The loaded halite-SiO_2 interface shows two different regions: contact area and non-contact area. In (a) the dry interface and in (b) the interface with saturated solution are shown. Regularly distributed indents are visible. Within the non-contact area Newton's rings can be seen. The images are reflected optical micrographs.

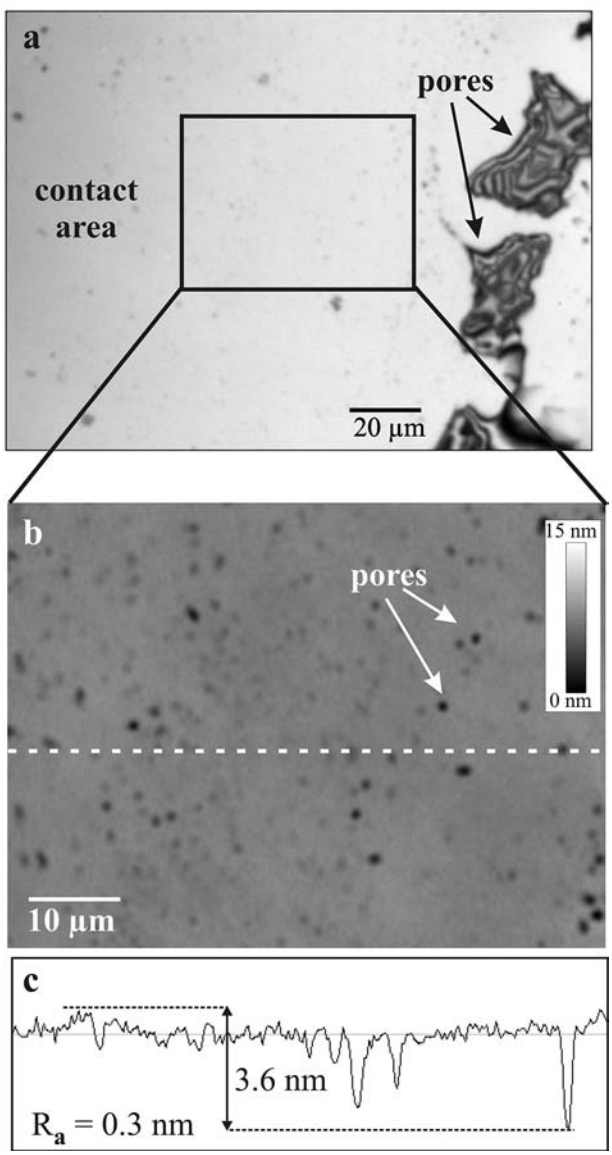

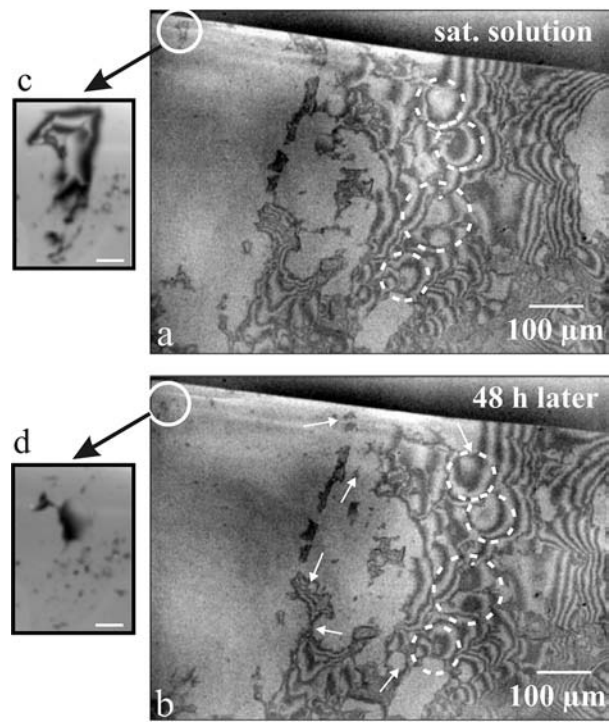

Fig. 5. The reflected optical micrographs (a) and (b) show the *in-situ* evolution of the loaded halite-SiO_2 interface in saturated solution at 30°C under constant load. The contact area broadens laterally (arrows). Some sites (dashed circles) show changes of Newton's rings from dark to bright and vice versa indicating a decrease of distance between the glass cover and the halite surface. (c) and (d) show the evolution of pores within the contact zone (scale bar = 10 µm).

Fig. 4. (a) Detail of the contact area (reflected optical micrograph). The depth of the large pores on the right side is about 1.3 µm. (b) The PSIM image shows small pores almost uniformly distributed over the contact area. The dashed line in (b) marks the position of the profile shown in (c).

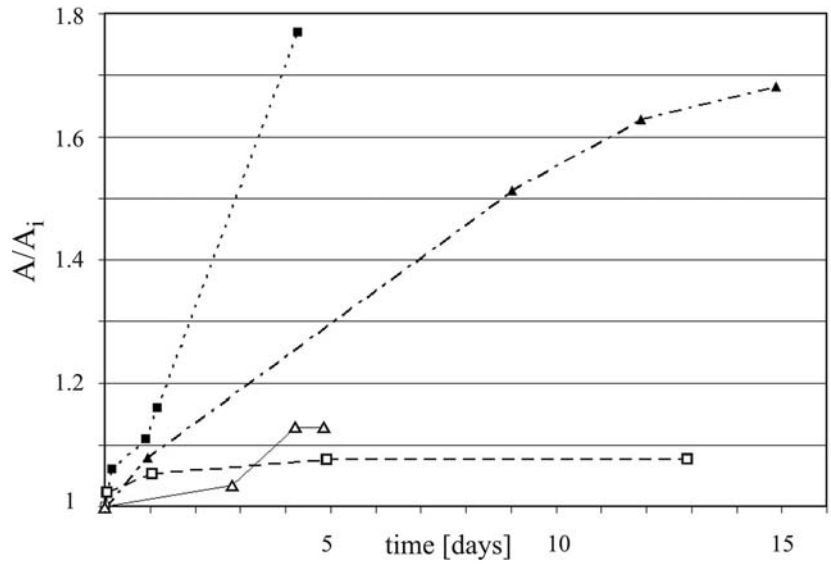

symbol	condition	load [N]	σ_i [MPa]	σ_f [MPa]
□	dry	3.5	26.9 ± 3	25 ± 3
△		7.7	89.5 ± 5.6	79.4 ± 4.8
■	wet	4.7	47.1 ± 6.2	26.6 ± 2.7
▲		7.7	68.1 ± 4	40.5 ± 2.2

Fig. 6. Ratio of the size A and the initial size A_i of the contact area plotted versus time (σ_i = initial stress, σ_f = final stress).

interface is 19.8 ± 2 MPa and 7 ± 1.8 MPa, respectively. Since the contact area is *ca*. 0.08 mm², the local stresses of 48.9 ± 5.8 MPa and 18.5 ± 6.3 MPa exceed the threshold for plastic deformation.

The non-contact area is characterized by Newton's rings as long as the distance between the SiO_2 surface and the halite surface is in the range of the coherence length of the light used. Beyond that distance, Newton's rings can not be seen. The smooth areas within the contact area have a roughness R_a of about 1 nm which is identical to the roughness of the SiO_2-coating. Therefore, most of this region can be assumed to be in physical contact. However, from PSIM measurements it is not possible to determine the actual interfacial distance in the contact area, *i.e.*, the thickness of a possible fluid film in the interface. Within the contact area pores were found. The size of the pores varies from the detection limit of PSIM (*ca.* 1 nm in depth and *ca*. 1 µm² in size) to a few hundreds of nm in depth and an area of about several hundreds of µm² (Fig. 4).

Evolution of the halite-SiO_2 interface under constant load

The morphological evolution of the interface under constant uni-axial load in saturated solution at 30°C is shown in Fig. 5. In this experiment, the applied uni-axial stress was 4.8 ± 0.6 MPa and 15.1 ± 0.1 MPa with respect to the total interface area (4 mm²) and the contact area (1.26 mm²), respectively. Within the interface, the contact area increased laterally (Fig. 5a and b) as indicated by arrows. In Fig. 6 the ratio of the size and initial size A/A_i of the contact area is plotted *versus* time for dry experiments (open symbols) and experiments with saturated solution (closed symbols). In the presence of fluid, the contact area increased by more than 50 % whereas dry experiments showed an increase in contact area of about 10 %. Besides the increase of contact area, also the non-contact area showed alterations induced by the applied stress. In Fig. 5a and b (marked with dashed circles), the interference patterns changed from dark to bright and *vice versa.* This change corresponds to a decrease of the interfacial spacing of about λ/4 (≈ 138 nm). The decrease can be caused by plastic deformation, by precipitation within the non-contact area, or by dissolution within the contact area, *i.e.*, the crystal is advancing towards the interface. However, the axial shape evolution of the entire crystal can be assessed independently by measuring the height difference between the levers beneath the cell. In Fig. 7a, the changes in axial length of a halite crystal is plotted *versus* time. With respect to the total interface area the stress was 1.5 ± 0.06 MPa. As opposed to the crystal convergence at dry conditions of about 0.9 µm within 15 days, in presence of saturated solution the convergence was approx. 7 µm within 30 days. When solution was added, the convergence first increased rapidly and then decelerated with time. Similar behaviour could be detected in the case of epoxy coated interfaces at a stress of 1.57 ± 0.1 MPa (Fig. 7b). As a reference, an experiment using a stack of SiO_2-glass plates was performed with a stress of 2.24 ± 0.1 MPa (Fig. 7c). Here, no axial convergence could be detected.

During lateral spreading of the contact area in solution, regions of the non-contact area can be enclosed by solid material creating fluid inclusions, some of which decreased

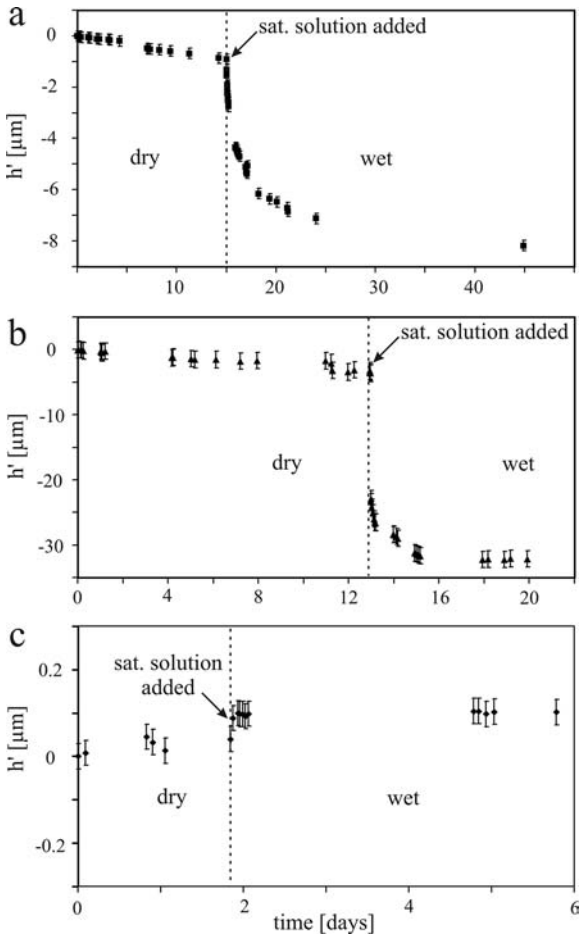

Fig. 7. Axial convergence *h*' of halite crystals with (a) uncoated interfaces and (b) epoxy coated interfaces. When saturated solution is added, the crystal length decreases. (c) shows a reference experiment using a stack of SiO_2-glass plates.

in size and depth subsequently (Fig. 5c and d). Initially existing small pores within the contact area with lateral dimensions of several µm² evolved in contrary ways. Quantitative evaluation of the time-dependence of the depth of the pores showed a decrease in depth of up to 2 ± 0.3 nm/day for 59 % of the investigated pores. About 25 % of the pores showed a decrease in depth of even up to 6.6 ± 0.4 nm/day. In contrast, the depth of nearly 10 % of the pores increased up to 2 ± 0.5 nm/day and *ca.* 6 % showed an increase of even up to 12 ± 0.6 nm/day.

In order to study the evolution of defined pores, Vickers indents were made on the (100) halite surface. At dry conditions, the indents did not show any significant change in size and depth when stress (up to 25 MPa) was applied. Figure 8a shows the interferogram of an indent in air on a free surface. The square edges of the indent were oriented parallel to <110> as the square edges of the Vickers pyramid base have been. In close proximity to the indent, bulges with a height of up to 400 nm were visible. Cracks could not be detected within the resolution limits. Adding *saturated* NaCl-solution caused dissolution of these plastically deformed regions of the indent. Within 30 minutes an etch pit was formed. However, the resulting square etch pit was oriented parallel to <100> in contrast to the original <110> indent (Fig. 8b). It further needs to be noted that the <100> orientation of etch pits was independent of the previous orientation of the indent. As expected, the indents within the non-contact area showed the same behaviour as on free surfaces. The plastically deformed regions of these indents dissolved forming etch pits as shown in Fig. 9. This was also the case for those indents, which were located within the contact area but temporarily had a clearly discernible connection to the bulk solution. However, the indents without any obvious contact to bulk solution did not form <100> etch pits, but were slowly filled with small crystals (Fig. 10). During the experiment, the apparent size of the indents successively decreased. Although six days later the indents became undetectable by *in-situ* microscopy (Fig. 10b to e), *ex-situ* investigations revealed that the indents still existed (Fig. 10f and g). The pyramidal pits were filled up with small crystals. Judging by their morphology, the new small crystals have a structural relation to the parental crystal but obviously did not directly grow at the indent walls which became irregular in shape. The length of the diagonal of the initial indent (approx. 19 µm) was found to be unchanged during the experiment. Important to note, the minimum distance between the indents filled with secondary crystals and the non-contact

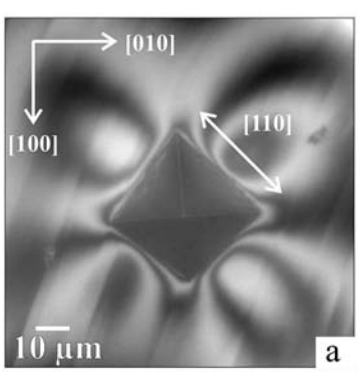

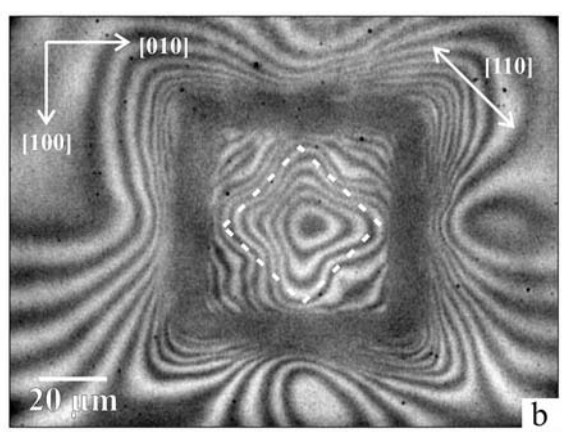

Fig. 8. (a) Interferogram of an indent on a halite surface. The edges of the square area are parallel <110>. The bulges surrounding the indent are clearly visible. Cracks can not be seen. The applied force was 0.2 N and the depth of the indent is *ca.* 6.3 µm. (b) *In-situ* interferogram after saturated solution has been added. The plastically deformed regions within and around the indent dissolved during 30 minutes. Now, the edges of the etch pit are parallel <100>. The dashed square marks the former position of the indent.

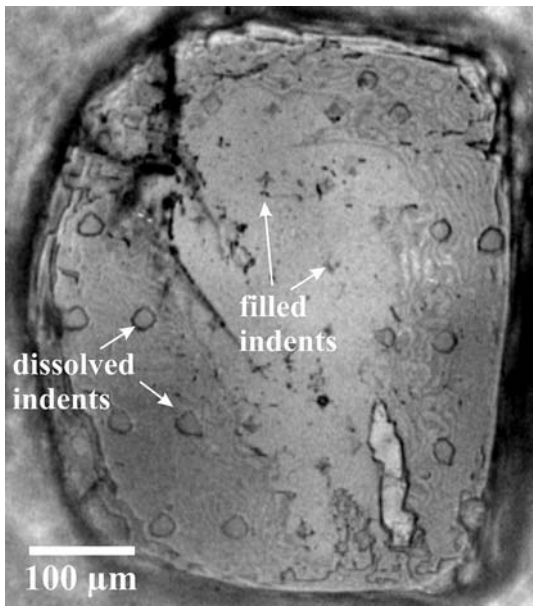

Fig. 9. Reflected light optical micrograph showing the interface of Fig. 3b *ca.* 3 hours later. The indents with a depth of *ca.* 2.8 µm within the non-contact area dissolved. Precipitation of material within indents of the contact area can be seen.

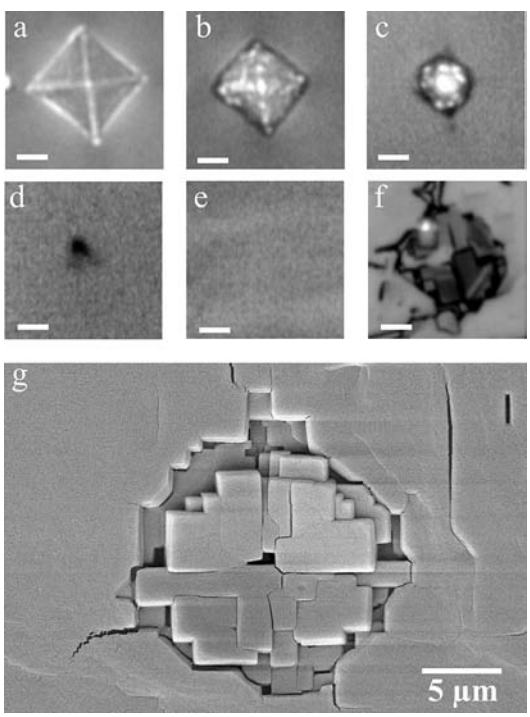

Fig. 10. (a) - (e) Evolution of an indent located within the contact area. (b) Precipitation of crystals becomes visible within the first hour. (c) Five hours later, a circle-like pore remains. (d) One day later, the diameter of the pore becomes smaller than 5 µm. (e) Six days later, the indent is no longer visible. (f) *Ex-situ* optical investigation after removing the cell cover reveals that the indent has been filled. (a) - (f) are reflected optical micrographs (scale bar = 5 µm). (g) SEM image of the filled indent.

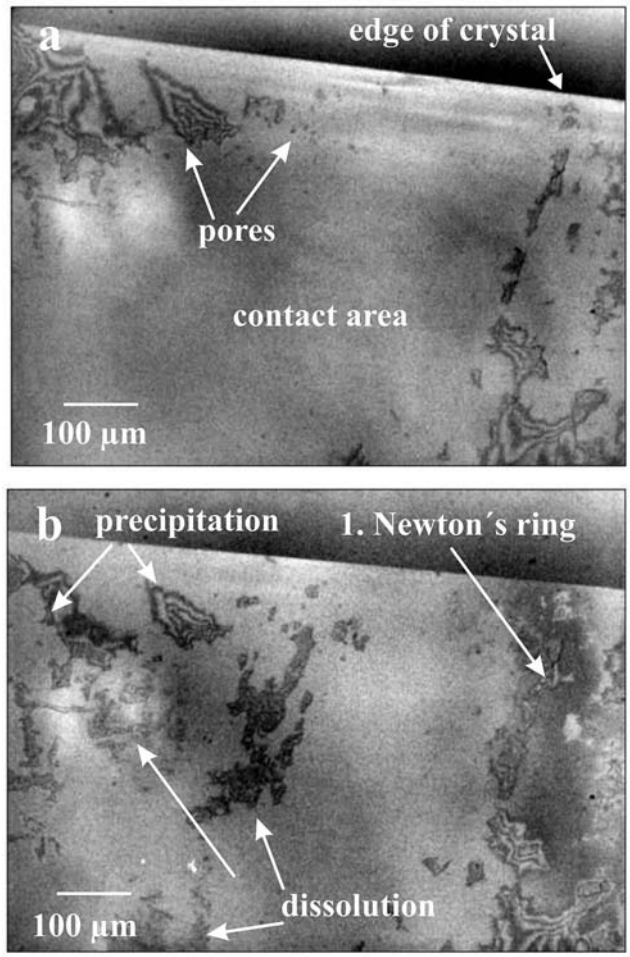

Fig. 11. Reflected optical micrographs of the halite-SiO_2 interface shown in Fig. 5. Unloading of the interface causes a decreasing size of the contact area and an increasing halite-SiO_2 distance in the non-contact area (see the new position of the first Newton's ring in 11b).

area was *ca.* 10 µm. Indents closer to the non-contact area behave like indents within the non-contact area.

Evolution of the halite-SiO_2 interface after unloading

In Fig. 11a, the halite-SiO_2 interface is shown under an uni-axial stress of approx. 15 MPa (with respect to the contact area of *ca.* 1.3 mm^2) applied for 8 days. Within this time frame, the typical evolution of the interface could be observed as described above. Unloading this interface caused a markedly different evolution of the interface. The reduction of stress to zero led to a lateral shift of the first Newton's ring (indicated in Fig. 11b) which is correspondent to a decrease in contact area and to an increase of the interfacial distance in the non-contact area. The measurements do not unequivocally reveal whether the previous contact areas are still in physical contact or if there is an interfacial gap smaller than $\lambda/4$ ($\approx$ 138 nm). Nevertheless, during one day new pores evolve (dark areas in Fig. 11b) which clearly show that dissolution has occurred within the

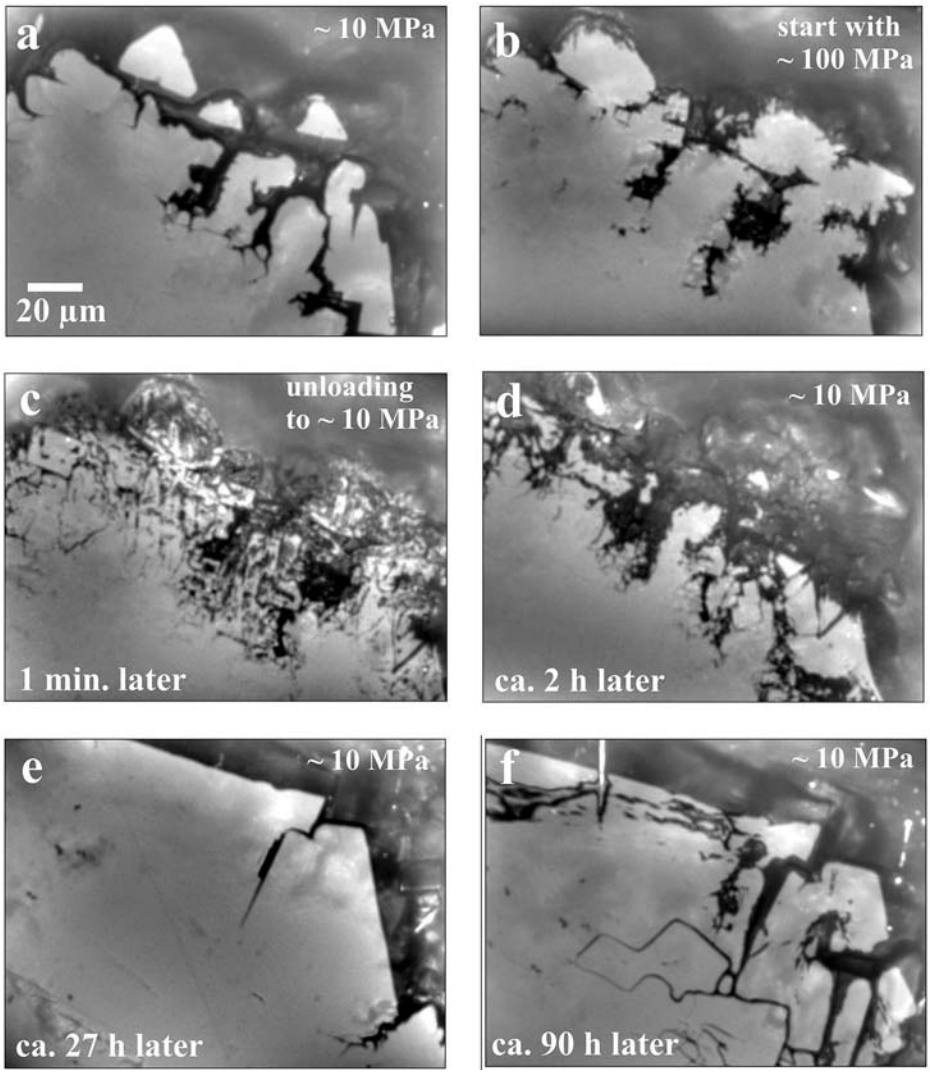

Fig 12. (a) Edge area of the halite-SiO_2 interface (reflected optical micrograph). (b) Increasing the stress to ~ 100 MPa led to spontaneous lateral broadening of the contact area. (c) After stress has again been reduced to ~ 10 MPa, dissolution started immediately. (d - f) Dissolution continued. (f) New crevices became visible.

contact area. Furthermore during this time frame, precipitation around the contact area occurred 200-300 µm away from the locations of dissolution.

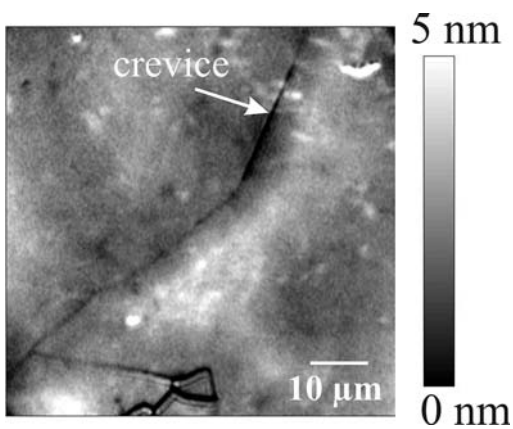

Fig. 13. PSIM image of the halite-SiO_2 interface after stress reduction to ~ 10 MPa showing depressions and crevices.

Evolution of the halite-SiO_2 interface during stress cycling

Figure 12 shows the evolution of the interface when the applied stress is episodically changed from *ca*. 100 MPa to *ca*. 10 MPa. In Fig. 12a, the halite-SiO_2 interface is shown as the stress has been reduced to 10 MPa for the second time. In Fig. 12b, the stress again has been increased to 100 MPa. The comparison of Fig. 12a and b shows, that the contact area increases probably due to plastic deformation of the halite crystal. Also, the crystal edge becomes frayed. After the stress again has been decreased to 10 MPa, within a few seconds rapid dissolution along the edge occurred forming a heavily pitted area (dark sites in Fig. 12c). Within the next hours, this pitted area slowly becomes removed and a new straight edge was formed (Fig. 12d to e). This new edge marks a smaller contact area due to dissolution of the plastically stressed material. In the course of the next few days, dissolution of the plastically deformed material continued by forming crevices into the contact area as shown in Fig. 12e and f. Figure 13 shows topographic details of the tip of a crevice protruding within the transition zone of non-contact to contact area. The

crevice in the image center has a depth of 1.5-3.5 nm, the depressions are about 2 nm deep as indicated by the dark areas on the left and right side.

Discussion

Dry stage

In the dry stage, a slow increase of the contact area and a slow axial convergence of the crystal can be detected under stress (Fig. 7a). The most likely process for this shape evolution is plastic deformation, *e.g.* by dislocation creep. According to Strumane & Dekeyser (1959), low temperature creep under constant load is activated at 2.5 MPa at 35°C and according to Wimmer *et al*. (1963) the critical resolved shear stress (CRSS) in air for freshly polished halite crystals is between 0.85 and 1.5 MPa at room temperature. Besides plastic deformation, dissolution-precipitation within capillary films might be involved.

Solution addition

When solution is added, deformation of the crystal is largely enhanced. If dissolution at the interface followed by transport of material out of the contact area was responsible for this deformation, both the top and the bottom interface of the crystal would contribute. Assuming similar behavior for both interfaces, the axial retreat within the experimental time frame is exceeding the depth of indents. The indents should have dissolved totally, but this was not the case. Therefore, we can infer that dissolution at the loaded surfaces does not dominantly contribute to the observed axial deformation. This finding is supported by the experiment employing epoxy-coated interfaces. Although in this experiment dissolution on the loaded surfaces can be neglected, the observed axial convergence was similar to the convergence in uncoated experiments. Thus when solution is added, deformation is not dominated by dissolution-precipitation processes but rather by accelerated dislocation creep. In solution, the strain rate of this deformation mechanism is well known to be increased and eventually results in an increased plasticity (Joffé *et al*., 1924; Smekal, 1928; Günther & Erdmann-Jesnitzer, 1956). In accordance to those authors, the period of increased deformation rate was finally followed by a rapidly abating axial convergence (Fig. 7).

The observed evolution of the contact area size with time is less clearly pronounced than the convergence. One reason is the larger experimental uncertainty in measuring the area size. Moreover temperature gradients, surface energy gradients or surface faceting can affect the contact area size in the presence of solution additionally to fluid-enhanced plastic deformation. Nevertheless, the observed data show analogous trends: during dry periods a slight increase in contact area size is followed by a more distinct increase when solution is added which finally decelerates again.

Indents and pores

Within the contact area, the shape evolution of initially existing pores is non-uniform. One important parameter here is the amount of plastically deformed material within the effective range of mass transport. Pores with constant shape may simply lack plastically deformed material within the range of transport. Another parameter in pore shape evolution is pore size. The saturation required for crystallization in pores with a size of about 1 μm is higher than for pores with a size of 100 μm (Putnis *et al*., 1995, Putnis & Mauthe, 2001).

However, the trend of the contact area towards gaining stability is also supported by the persistent existence and shape of the indents within the contact area, which just become filled by crystals. Unlike the indents in the non-contact area, the indents in the contact area do not change, *i.e*., plastically deformed material within the indents is not removed and transported out of the interface. This hampered transport can also be perceived by the behaviour of interfaces under episodically changed loads. Fast transport of material, which was deformed within the contact area by the anterior high-load-stage, is activated by decreasing the load (see Fig. 12). Unfortunately, PSIM is not able to exactly determine the equilibrium distance within the contact area of the two solids under the reduced load. A detailed evaluation of the transport conditions within the interface under reduced load therefore still remains open. However, the typical distance of transport can be estimated from the behavior of indents depending on their distance to the non-contact area. Indents, which have discernible connection to bulk fluid or which lie within a distance of 10 μm to the non-contact area, dissolve until they obtain <100> etch pit morphology. Indents do not convert into etch pits when their distance to obvious non-contact areas exceeds about 10 μm. For the contact area we therefore can infer that within the experimental time frame mass transport over distances exceeding 10 μm is not effective.

Because of this limited effective range of mass transport within the contact area, the material sources for the new crystals within the indents are most likely the bulges of plastically deformed material around the indents. The indents can therefore be considered as micro-systems for an evaluation of the processes involved in DPC. Advantageous in using these micro-systems is the short path length of material transport from areas with a higher chemical potential of the constituent components in the solution (here: the loaded interface containing plastically deformed material at the indent) to areas with lower chemical potential. This short path length ensures that kinetic restraints by mass transport are less important within the experimental time frame. Detailed inspection of the filled indents shows that the crystals have a crystallographic relation to the parental crystal but the crystals do not grow at the walls of the indent, they rather grow towards the wall. This shows that material which is dissolved at the stressed parental crystal prefers to grow at new nuclei within the indent rather than at the free surfaces of the stressed indent wall. The topotactic relation between the parental crystal

and the new small crystals points towards a nucleation at a few sites of the parental crystal which offer energetically favorite conditions. Elsewhere at the indent wall, the conditions for growth are energetically less favorable than on the surface of the nucleated new crystals. The indent wall merely shows some faceting to minimize surface energy and the dislocation-related internal energy - the indent diameter does not decrease significantly.

Driving forces

DPC is assumed to be driven by potential energy *via* the work term in Eqn. 2 exclusively. However, plastic deformation of material causes a considerable increase in internal energy. The indents as DPC-micro-systems show that this increased internal energy increases the chemical potential and the supersaturation with respect to the hydrostatic state. However, the resulting deformation still strongly depends on the effective kinetic constraints and on energy gradients both within individual crystals and within the accessible system.

Remarkably different to DPC in steady state systems as described above is the situation when the chemical potential has an even small contribution of a permanently increased internal energy (*e.g.* by plastic deformation) *and* temporarily reduced transport constraints (*e.g*. by periods of reduced load). Thus, unlike the work term any permanent increase in internal energy can take advantage of the increased transport capability during periods of decreased load. Temporary reduction of anisotropic stress can therefore provide an efficient way to drive transport in DPC. In this way, small contributions to internal energy can by far outrange the effect of the work term on DPC and thus may be a very important factor for deformation in natural systems.

Interface morphology

Hickman & Evans (1991) reported no evidence for an island-channel morphology at optical resolution and provided the model of a continuous fluid film with a maximum thickness of about 30 nm, because the loads in their experiments were sufficient to cause fully plastic deformation of the contact zone. In contrast, Schutjens & Spiers (1999) reported that initial application of normal stress induces instantaneous formation of a rough contact morphology composed of islands and channels in a length scale of several micrometers. This initial roughness was reported to evolve into an optically flat region while shortening of the crystal continued. However as can be seen by the behaviour of pores and indents within the contact area in our experiments, nano-scale voids or cavities remain stable and therefore favor an interface morphology that will not become perfectly smooth and may rather be described by the island-channel model. Since the size of the contact area in an island-channel interface morphology is always smaller than the entire interface area, this type of interface morphology may also be conducive to small but recurring contributions of plastic deformation to the internal energy of the anisotropically stressed crystal.

Conclusions

The deformation rate of halite is significantly increased by the addition of aqueous solution compared to dry conditions. The dominant mechanism is plastic deformation rather than convergence by dissolution-retreat of loaded faces.

Dissolution occurs rapidly where material is subject to local plastic deformation at point contacts (and at concentrations of elastic energy). The dissolved material preferentially reprecipitates in larger pores and voids in hydrostatic conditions. According to Gibbs, the reprecipitation in hydrostatic conditions is the thermodynamic optimum. Competing sinks such as growth at grain-to-pore interfaces of the stressed crystal will be significant only in the case of an inaccessible thermodynamic optimum.

Within the loaded contacts in grain-to-grain interfaces, the range of transport of dissolved material is limited depending on the time scale. After the directly accessible space for hydrostatic precipitation has been exhausted in geological systems, dissolution-precipitation processes driven by $(\sigma_n - p)v_p$ alone will be subjected to increasing transport constraints. A possible mechanism for sustained dissolution-precipitation creep is the cyclic variation of external parameters like stress. In the phase of stress relaxation the transport capabilities can be increased and further space for hydrostatic precipitation is generated. Thus, cyclic or recurrent loading can assist to dissipate supersaturated solutions caused by remanent energy contributions such as increased internal energy due to plastic deformation during high stress episodes. Dissolution-precipitation creep has commonly been assumed to be a steady state process so far. From our investigations we can infer that cyclic build up and release of stress as evident in seismic activities can become a key factor for fluid assisted deformation of rocks.

Acknowledgement: The work would not have been possible without the help of G. Andersen and W. Schrimpf in the design and their skilful construction of the cell. We also wish to thank M. Blüm for the preparation of the indents and B. Stöckhert for fruitful discussions and improving the manuscript. This work was funded by Deutsche Forschungsgemeinschaft (Sonderforschungsbereich 526).

References

Bos, B., Peach, C.J., Spiers, C.J. (2000): Frictional-viscous flow of simulated fault gouge caused by the combined effects of phyllosilicates and pressure solution. *Tectonophysics*, **327**, 173-194.

Cox, S.F. & Paterson, M.S. (1991): Experimental dissolution-precipitation creep in quartz aggregates at high temperatures. *Geophys. Res. Lett.*, **18**, 1401-1404.

de Meer, S., Spiers, C.J., Peach, C.J. (2000): Kinetics of precipitation of gypsum and implications for pressure-solution creep. *J. geol. Soc. London*, **157**, 269-281.

den Brok, S.W.J. (1998): Effect of microcracking on pressure-solution strain rate: The Gratz grain-boundary model. *Geology*, **26**, 915-918.

den Brok, S.W.J. & Morel, J. (2001): The effect of elastic strain on the microstructure of free surfaces of stressed minerals in contact with an aqueous solution. *Geophys. Res. Lett.*, **28**, 603-606.

den Brok, S.W.J., Zahid, M., Passchier, C.W. (1999): Pressure solution compaction of sodium chlorate and implications for pressure solution in NaCl. *Tectonophysics*, **307**, 297-312.

Durney, D.W. (1972): Solution-transfer, an important geological deformation mechanism. *Nature*, **235**, 315-317.

Dysthe, D.K., Podladchikov, Y., Renard, F., Feder, J., Jamtveit, B. (2002): Universal Scaling in Transient Creep. *Phys. Rev. Lett.*, **89**, 246102-1-4.

Gibbs, J.W. (1906): On the equilibrium of heterogeneous substances. *in*: "The collected works of J. Willard Gibbs", **1**, Yale Univ. Press, New Haven, 184-201.

Giles, A. (1932): Textural features of the Ordovician sandstones of Arkansas. *J. Geol.*, **40**, 97-118.

Gratier, J.-P., Renard, F., Labaume, P. (1999): How pressure solution creep and fracturing processes interact in the upper crust to make it behave in both a brittle and viscous manner. *J. Struct. Geol.*, **21**, 1189-1197.

Günther, F. & Erdmann-Jesnitzer, F. (1956): Zur Plastizität benetzter Sylvin- und Steinsalzkristalle. *Z. Elektrochem.*, **60**, 85-93.

Heald, M.T. (1956): Cementation of Simpson and St. Peter sandstones in parts of Oklahoma, Arkansas and Missouri. *J. Geol.*, **64**, 16-30.

Hickman, S.H. & Evans, B. (1991): Experimental pressure solution in halite: the effect of grain/interphase boundary structure. *J. geol. Soc. London*, **148**, 549-560.

—,— (1995): Kinetics of pressure solution at halite-silica interfaces and intergranular clay films. *J. Geophys. Res.*, **100**, No. B7, 13,113-13,132.

Joffé, A., Kirpitschewa, M.W., Lewitzky, M.A. (1924): Deformation und Festigkeit der Kristalle. *Z. Phys.*, **22**, 286-302.

Lehner, F.K. (1995): A model for intergranular pressure solution in open systems. *Tectonophysics*, **245**, 153-170.

Lohkämper, T.H.K., Jordan, G., Costamagna, R., Stöckhert, B., Schmahl, W.W. (2003): Phase shift interference microscope study of dissolution-precipitation processes of nonhydrostatically stressed halite crystals in solution. *Contrib. Mineral. Petrol.*, **146**, 263-274.

Martin, B., Röller, K., Stöckhert, B. (1999): Low-stress pressure solution experiments on halite single-crystals. *Tectonophysics*, **308**, 299-310.

McClay, K.R. (1977): Pressure solution and Coble creep in rocks and minerals: a review. *J. Geol. Soc. London*, **134**, 57-70.

Ostapenko, G.T. (1968): Recrystallization of minerals under stress. *Geochem. Intern.*, **5**, 183-186.

Paterson, M.S. (1973): Nonhydrostatic thermodynamics and its geologic applications. *Rev. Geophys. Space Phys.*, **11**, 355-389.

Putnis, A. & Mauthe, G. (2001): The effect of pore size on cementation in porous rocks. *Geofluids*, **1**, 37-41.

Putnis, A., Prieto, M., Fernandez-Diaz, L. (1995): Fluid supersaturation and crystallization in porous media. *Geol. Mag.*, **132**, 1-13.

Raj, R. (1982): Creep in polycrystalline aggregates by matter transport through a liquid phase. *J. Geophys. Res.*, **87**, 4731-4739.

Raj, R. & Chyung, C.K. (1981): Solution-precipitation creep in glass ceramics. *Acta Metall.*, **29**, 159-166.

Rutter, E.H. (1976): The kinetics of rock deformation by pressure solution. *Phil. Trans. R. Soc. Lond. A*, **283**, 203-219.

Sandoz, P. (1996): An algorithm for profilometry by white-light phase-shifting interferometry. *J. Mod. Optics*, **43**, 1545-154.

Schutjens, P.M.T.M. & Spiers, C.J. (1999): Intergranular pressure solution in NaCl: Grain-to-grain contact experiments under the optical microscope. *Oil Gas Sci. Techn. - Rev. IFP*, **54**, 729-750.

Schwarz, S. & Stöckhert, B. (1996): Pressure solution in siliciclastic HP-LT metamorphic rocks - constraints on the state of stress in deep levels of accretionary complexes. *Tectonophysics*, **255**, 203-209.

Sinha-Roy, S. (2002): Kinetics of differentiated stylolite formation. *Current Science*, **82**, 1038-1046.

Sheldon, H.A., Wheeler, J., Worden, R.H., Cheadle, M.J. (2003): An analysis of the roles of stress, temperature, and pH in chemical compaction of sandstones. *J. Sed. Res.*, **73**, 64-71.

Shimizu, I. (1995): Kinetics of pressure solution creep in quartz: theoretical considerations. *Tectonophysics*, **245**, 121-134.

Smekal, A. (1928): Joffés Untersuchungne über die elektrische Durchschlagsfestigkeit. *Naturwissenschaften*, **16**, 743-744.

Sorby, H.C. (1863): Über Kalkstein-Geschiebe mit Eindrücken. *N. Jb. Min. Geol. Paläont.*, 801-807.

Spiers, C.J. & Schutjens, P.M.T.M. (1990): Densification of crystalline aggregates by fluid-phase diffusional creep. *in*: "Deformation processes in minerals, ceramics and rocks", Barber, D.J. & Meredith, P.G., ed. Unwin Hyman, *London*, 334-353.

Spiers, C.J., Schutjens, P.M.T.M., Brzesowsky, R.H., Peach, C.J., Liezenberg, J.L., Zwart, H.J. (1990): Experimental determination of constitutive parameters governing creep of rocksalt by pressure solution. *in*: "Deformation Mechanisms, Rheology and Tectonics", Knipe, R.J. & Rutter, E.H., ed. London, **54**, 215-227.

Stöckhert, B. Wachmann, M., Küster, M., Bimmermann, S. (1999): Low effective viscosity during high pressure metamorphism due to dissolution precipitation creep: the record of HP-LT metamorphic carbonates and siliciclastic rocks from Crete. *Tectonophysics*, **303**, 299-319.

Strumane, R. & Dekeyser, W. (1959): Low temperature creep of rock salt single crystals. *Acta Metallurgica*, **7**, 520-521.

Trurnit, P. (1968): Pressure solution phenomena in detrital rocks. *Sediment. Geol.*, **2**, 89-114.

Urai, J.L., Spiers, C.J., Zwart, H.J., Lister, G.S. (1986): Weakening of rock salt by water during long-term creep. *Nature*, **324**, 554-557.

Weyl, P.K. (1959): Pressure solution and the force of crystallisation - A phenomenological theory. *J. Geophys. Res.*, **64**, 2001-2025.

Wimmer, F.T., Kobes, W., Fine, M.E. (1963): Tensile Properties of NaCl-BaNr Solid Solution Single Crystals. *J. Appl. Phys.*, **34**, 1175-1778.

Received 8 May 2004
Modified version received 10 November 2004
Accepted 6 December 2004